ATLAS CONF Note

ATLAS-CONF-2022-023

5th April 2022

Correlation of Υ meson production with the underlying event in pp collisions measured by the ATLAS experiment

The ATLAS Collaboration

The multiplicity and distributions of kinematic variables of charged particles produced in association with an Υ meson are measured in proton-proton collisions using the data collected by the ATLAS experiment at the LHC. The analysis uses a full Run 2 data set at $\sqrt{s}$ = 13 TeV, corresponding to the integrated luminosity of 139 fb^{-1}. The measurement is performed separately for the first three Υ (nS) states in several intervals of Υ transverse momenta. At Υ transverse momentum close to zero, the associated charged-particle multiplicity is measured to be smaller by 12 ± 1% in collisions where Υ (2S) is observed compared to the collisions with Υ (1S). For Υ (3S) this difference is 17 ± 4%. These differences decrease with increasing transverse momentum of the Υ states.

ATLAS-CONF-2022-023
11 April 2022

1 Introduction

Correlations between processes characterized by different momentum scales and correlations between "hard" and "soft" particle production are interesting but relatively unexplored aspects of high-energy collisions. This topic lies at the intersection of several research directions pursued in the high-energy and heavy-ion research programs at the LHC. The underlying event (UE) is an important feature of proton-proton (pp) collisions and is essential to determine the role that multiparton interactions play in the formation of the final state. Color fields connect all the strongly interacting partons and so an unambiguous assignment of particles to the hard scattering partons or UE is not possible. Despite this ambiguity, observables such as the multiplicity, transverse momentum, and angular distributions of charged particles are sensitive to the UE [1–3]. In the context of heavy-ion physics, the UE may reflect the conditions for Quark-Gluon Plasma (QGP) formation and may also be used as a metric of event activity.

Heavy-flavor (HF) production in high-energy collisions is a sensitive test of our understanding of QCD in pp collisions. Several measurements of $\Upsilon(n\mathrm{S})$ mesons in pp collisions at the LHC [4–11] have been performed and these have spurred the development of refined models based of perturbative QCD (see a recent review in [12] and references therein). In addition, the Υ meson is a probe which is expected to undergo energy loss in the hot dense medium formed in A + A collisions. Based on lattice-QCD calculations, it is expected that in a QGP medium heavy quarkonium states will be "sequentially suppressed" as the deconfined color charges within the QGP will screen the heavy $q\bar{q}$ pair (see a review in Ref. [13] and references therein). Analyzing the correlation between the UE and HF meson formation can provide information about density and screening of color charges in the produced matter as a function of the size of the produced system.

The CMS collaboration has measured the event activity dependence of the relative production of $\Upsilon(n\mathrm{S})$ states in pp collisions [14, 15]. Event activity was represented by charged-particle multiplicity. In these studies, it was observed that the ratios of $\Upsilon(2\mathrm{S})$ to $\Upsilon(1\mathrm{S})$ and $\Upsilon(3\mathrm{S})$ to $\Upsilon(1\mathrm{S})$ production cross-sections decrease as a function of the charged particle multiplicity, and more charged particles are present in events with an observed $\Upsilon(1\mathrm{S})$ than events with observed $\Upsilon(2\mathrm{S})$ or $\Upsilon(3\mathrm{S})$. Furthermore, the relative $\Upsilon(n\mathrm{S})$ production in different event topologies, as quantified by the transverse sphericity dependence, suggested that the differences between $\Upsilon(n\mathrm{S})$ states are not simply a function of their mass differences, and are not due to effects of jets that balance the $\Upsilon(n\mathrm{S})$ momentum. Reference [15] hypothesized that this might be consistent with a suppression of the excited Υ states at high charged-particle multiplicity.

The present analysis measures the multiplicity and kinematic distributions of inclusive charged particles in pp collisions where $\Upsilon(n\mathrm{S})$ meson is produced. The $\Upsilon(n\mathrm{S})$ mesons are reconstructed from their decay to oppositely charged muon pairs. Charged particle observables are corrected for pile-up (PU) contamination, the effect caused by multiple pp collisions in a single LHC bunch crossing, following the approach of Ref. [16]. The distributions of the azimuthal angle between the charged particles and the Υ meson ($\Delta\phi$), as well as the charged particle transverse momentum (p_{T}) are measured as functions of the $\Upsilon(n\mathrm{S})$ state and its transverse momentum $p_{\mathrm{T}}^{\mu\mu}$. In this analysis, the UE is characterized by the collection of charged particles not directly involved in the formation of the Υ state produced in the collision.

2 ATLAS detector

The ATLAS detector [17] at the LHC covers nearly the entire solid angle around the collision point.[1] It consists of an inner tracking detector surrounded by a thin superconducting solenoid, electromagnetic and hadron calorimeters, and a muon spectrometer incorporating three large superconducting air-core toroidal magnets.

The inner-detector system (ID) is immersed in a 2 T axial magnetic field and provides charged-particle tracking in the range $|\eta| < 2.5$. The high-granularity silicon pixel detector covers the vertex region and typically provides four measurements per track, the first hit normally being in the insertable B-layer (IBL) installed before Run 2 [18, 19]. It is followed by the silicon microstrip tracker (SCT), which usually provides eight measurements per track. These silicon detectors are complemented by the transition radiation tracker (TRT), which enables radially extended track reconstruction up to $|\eta| = 2.0$. The TRT also provides electron identification information based on the fraction of hits (typically 30 in total) above a higher energy-deposit threshold corresponding to transition radiation.

The calorimeter system covers the pseudorapidity range $|\eta| < 4.9$. Within the region $|\eta| < 3.2$, electromagnetic calorimetry is provided by barrel and endcap high-granularity lead/liquid-argon (LAr) calorimeters, with an additional thin LAr presampler covering $|\eta| < 1.8$ to correct for energy loss in material upstream of the calorimeters. Hadron calorimetry is provided by the steel/scintillator-tile calorimeter, segmented into three barrel structures within $|\eta| < 1.7$, and two copper/LAr hadron endcap calorimeters. The solid angle coverage is completed with forward copper/LAr and tungsten/LAr calorimeter modules optimised for electromagnetic and hadronic energy measurements respectively.

The muon spectrometer (MS) comprises separate trigger and high-precision tracking chambers measuring the deflection of muons in a magnetic field generated by the superconducting air-core toroidal magnets. The field integral of the toroids ranges between 2.0 and 6.0 T m across most of the detector. Three layers of precision chambers, each consisting of layers of monitored drift tubes, covers the region $|\eta| < 2.7$, complemented by cathode-strip chambers in the forward region, where the background is highest. The muon trigger system covers the range $|\eta| < 2.4$ with resistive-plate chambers in the barrel, and thin-gap chambers in the endcap regions.

Interesting events are selected by the first-level trigger system implemented in custom hardware, followed by selections made by algorithms implemented in software in the high-level trigger (HLT) [20]. The first-level trigger accepts events from the 40 MHz bunch crossings at a rate below 100 kHz, which the high-level trigger further reduces in order to record events to disk at about 1 kHz.

An extensive software suite [21] is used in the reconstruction and analysis of real and simulated data, in detector operations, and in the trigger and data acquisition systems of the experiment.

[1] ATLAS uses a right-handed coordinate system with its origin at the nominal interaction point (IP) in the centre of the detector and the z-axis along the beam pipe. The x-axis points from the IP to the centre of the LHC ring, and the y-axis points upwards. Cylindrical coordinates (r, ϕ) are used in the transverse plane, ϕ being the azimuthal angle around the z-axis. The pseudorapidity is defined in terms of the polar angle θ as $\eta = -\ln\tan(\theta/2)$. The rapidity is defined as $y = \frac{1}{2}\ln[(E + p_z)/(E - p_z)]$, where E is the energy of a particle and p_z is the momentum component in the beam direction.

3 Analysis

The analysis uses the entire Run-2 $\sqrt{s}$ = 13 TeV pp dataset with an integrated luminosity of 139 fb^{-1} obtained by the ATLAS experiment in 2015–2018. Data used in the analysis is drawn from data-taking periods during which the colliding beams and detector operations were stable [22]. For the measurement of per-event quantities performed in this analysis, data is further selected to ensure that the instantaneous luminosity is accurately determined and that the position and size of the interaction region are stable. These selections are required for the PU correction, which is performed as described in a previous ATLAS analysis [16]. Run periods in which there are 50 or more average simultaneous interactions in ATLAS are excluded.

To correct for detector effects, Pythia 8 [23] Monte-Carlo (MC) simulation samples with A14 tune and CTEQ6L1 parton distribution function [24] are used. Pythia 8 is complemented by the PHOTOS package [25, 26] to simulate the effects of final-state radiation. The detector response in the MC samples is simulated under similar PU conditions as in the data using Geant4 [27, 28], and the resulting events are reconstructed using the same algorithms that are applied to the data. In addition to the fully reconstructed simulation sample, a high statistics generated particle level sample of Pythia 8 was produced with the same tune. Another Pythia 8 sample was produced at generator level, with the color reconnection scheme changed from the default to a scheme which takes into account the full QCD color configuration in the beam remnant [29] as a cross-check.

Data used in the analysis is obtained using several di-muon HLTs with different thresholds applied on muon momentum p_{T}^{μ} ranging from 4 to 11 GeV [30, 31]. Different triggers were employed during different periods, and some of them recorded only a fraction of the instantaneous luminosity due to trigger pre-scale factors. This analysis uses all the relevant di-muon triggers, each event is assigned to only one trigger by matching reconstructed muons to HLT objects using standard ATLAS tools [32].

The analysis is based on the selection and reconstruction of $\Upsilon \rightarrow \mu^{+}\mu^{-}$ events and measurement of charged particle multiplicity and distributions of kinematic variables in these events. Extracted charged particle distributions are corrected for detector effects by applying weights on an event-by-event and particle-by-particle basis that are derived from simulated events by comparing particle and detector level distributions [3]. The analysis is performed in intervals of $p_{\mathrm{T}}^{\mu\mu}$, and the results are corrected for the contribution from the PU background.

In the offline analysis, muons are reconstructed as combined tracks spanning both the ID and the MS. Muons are required to fall within the fiducial acceptance of the ATLAS detector, defined as $p_{\mathrm{T}}^{\mu} > 4$ GeVand $|\eta^{\mu}| < 2.4$. This offline selection is used for the data obtained with the lowest muon p_{T} trigger. For the data samples obtained with higher muon-p_{T} triggers, the offline selection uses higher p_{T} values, matching the nominal momentum of the trigger. Tight quality requirements are imposed on the muon track both in the ID and MS to suppress backgrounds [33]. Muons associated with a common vertex must have longitudinal impact parameter less than 0.5 mm, and the significance of the transverse impact parameter is required to be less than 3.

Events with two oppositely charged muons which satisfy these criteria and are matched to HLT objects are selected for analysis. The muons are required to form a pair with invariant mass in the interval $8.2 \leq m^{\mu\mu} < 11.8$ GeV, and within the rapidity $|y^{\mu\mu}| < 1.6$. The rapidity condition is used to avoid detector regions where the acceptance is different for different $\Upsilon(n\mathrm{S})$ states.

The factors which determine whether the ATLAS detector reconstructs the Υ meson are the fiducial acceptance, muon reconstruction efficiency, and di-muon trigger efficiency. The muon reconstruction efficiencies and di-muon trigger efficiencies are obtained using simulated events. The muon reconstruction efficiency is defined as the product of the probability of a muon reconstructed as an ID track to also be reconstructed in the MS and the probability that a muon is reconstructed as an ID track [33]. The latter cannot be measured directly and is replaced by the conditional probability that a muon reconstructed by the MS is also reconstructed by the ID independently. To cover possible differences between data and simulation, the efficiency values calculated in simulation are corrected by scale factors which are the ratios of measured and simulated efficiencies obtained using the tag-and-probe method [30, 33].

The trigger inefficiency for a di-muon pair factorizes as the product of the two single muon trigger efficiencies, a term which depends on the distance between two muons, and a term that accounts for the loss due to online cuts applied to a pair, such as on the invariant mass, vertex fit quality, etc. [31]. The efficiencies are obtained from MC simulation and are corrected by the corresponding scale factors.

The fiducial acceptance for $\Upsilon \to \mu\mu$ decays is defined as the probability that the decay products fall within the fiducial volume, characterized by p_{T}^{μ} and η^{μ} thresholds, for a given transverse momentum and rapidity of an $\Upsilon(n\mathrm{S})$ state. The fiducial acceptance correction is evaluated from a fast MC simulation of $\Upsilon(n\mathrm{S})$ decays and applied as a weight to a dimuon pair with the corresponding reconstructed values of $p_{\mathrm{T}}^{\mu\mu}$ and $y^{\mu\mu}$ in 0.1 GeV-wide slices of $m^{\mu\mu}$. Triggers are corrected to a fiducial acceptance corresponding to the nominal values of the trigger thresholds.

Only primary charged particles, with p_{T} between 0.5 and 10 GeV, and $|\eta| < 2.5$, are considered in the analysis. These are defined as particles with average lifetime $\tau > 0.3 \times 10^{-10}$s and produced directly in the interaction or those from decays of particles with a shorter lifetime. Charged particles are identified as tracks reconstructed in the ID. Tracks are required to pass a set of quality requirements in the ID according to the track reconstruction model [34], and to have p_{T} and η in the same range defined as the charged particle acceptance. Muon tracks coming from Υ decays are used only to reconstruct the Υ state and not counted as charged particles. Correction weights applied to the tracks account for two factors, the probability of the track to be lost and the probability of the track to be produced by a non-primary particle. The weights are derived from simulated events, and their dependence on track p_{T}, η, and the di-muon vertex position is taken into account. The vertex position is considered because PU conditions are sensitive to it. Only tracks which fall within 0.5 mm from the averaged vertex position in the transverse direction and within 0.75 mm from the position of the vertex associated with muons in longitudinal directions are considered. The latter conditions significantly reduce the number of PU tracks selected for the analysis, but do not eliminate them completely. Following the analysis detailed in Ref. [16], an additional event sample is created which contains events identical to the PU component present in the data. These events are used to correct PU contributions to the analysis.

An example of the invariant mass distribution of the muon pair is shown in the left panel of Figure 1. It is fitted to a function that contains contributions for signal and background; the latter is predominantly composed of di-jets and Drell-Yan.

$$\begin{aligned} \text{fit}\,(m) &= \sum_{n\mathrm{S}} N_{\Upsilon(n\mathrm{S})} F_n(m) + N_{\mathrm{bkg}} F_{\mathrm{bkg}}(m) \\ F_n(m) &= (1-\omega_n) CB_n(m) + \omega_n G_n(m) \\ F_{\mathrm{bkg}}(m) &= \sum_{i=0}^{3} a_i (m-m_0)^i ; a_0 = 1 \end{aligned} \tag{1}$$

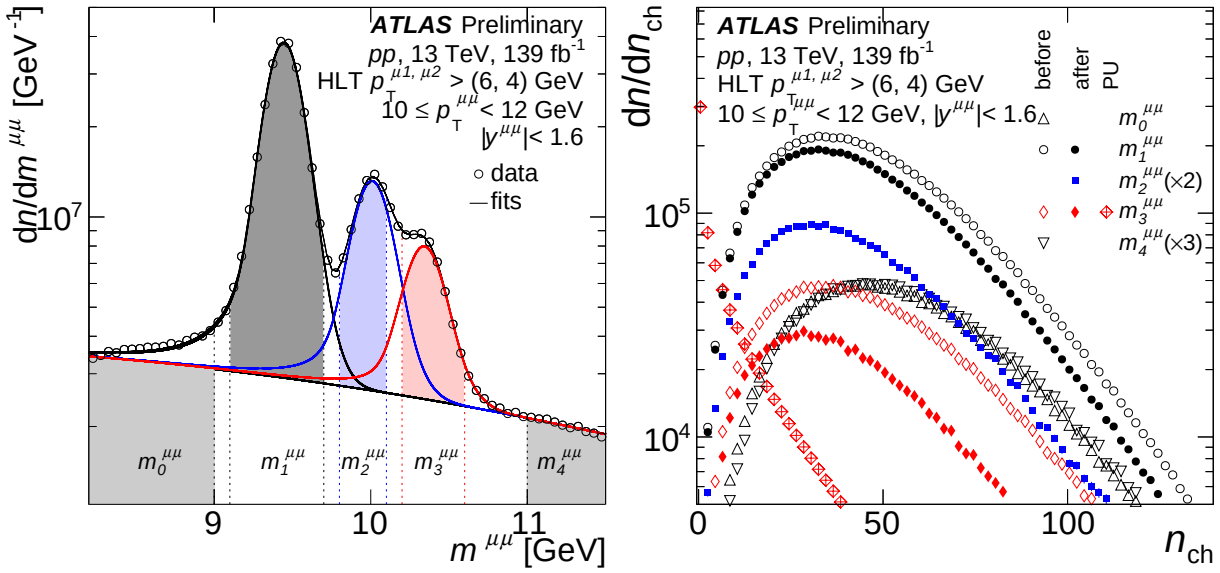

Figure 1: Left: Invariant mass distribution measured in the data in a $10 \leq p_{\mathrm{T}}^{\mu\mu} < 12$ GeV interval of the di-muon pair, fitted to the function used for extracting $\Upsilon(n\mathrm{S})$ yields. Indices 0 – 4 denote $m^{\mu\mu}$ intervals used in the analysis. Right: Several n_{ch} distributions measured in the mass intervals indicated in the left panel. Open markers are distributions before subtracting the background are shown for 4 $m^{\mu\mu}$ intervals out of 5. Full markers are distributions after subtracting the background are shown for 3 mass intervals. Hatched markers indicate n_{ch} distribution coming from the PU that is measured in $m_3^{\mu\mu}$. PU distributions have the same shape in all intervals.

where index n corresponds to three $\Upsilon(n\mathrm{S})$ states. $N_{\Upsilon(n\mathrm{S})}$ are the yields of the $\Upsilon(n\mathrm{S})$ states and N_{bkg} is the background normalization coefficient. CB is the Crystal Ball p.d.f., G is a Gaussian p.d.f., the coefficient ω is responsible for the relative contribution of these two p.d.f.'s, and the function F_{bkg} which is responsible for the background is the third degree polynomial whose constant coefficient is set to unity. It is centered at $m_0 = 10$ GeV, which approximately corresponds to the center of the fitting region. The CB is a modification of the Gaussian function with the power-law tail at low masses that is intended to accommodate the effects of final-state radiation:

$$
\begin{aligned}
CB\left(m;\mu_0,\sigma,\alpha,p\right) &= N\cdot\begin{cases}\exp\left(-\frac{1}{2}\cdot\left[\frac{m-\mu_0}{\sigma}\right]^2\right), & \left[\frac{m-\mu_0}{\sigma}\right] > -\alpha\\ A\left(B-\left|\frac{m-\mu_0}{\sigma}\right|\right)^{-p}, & \left[\frac{m-\mu_0}{\sigma}\right] \leq -\alpha\end{cases} \qquad (2)\\
A &= \left(\frac{p}{|\alpha|}\right)^p\cdot\exp\left(-\frac{|\alpha|^2}{2}\right)\\
B &= \frac{p}{|\alpha|}-|\alpha|\\
N &= \frac{1}{\sigma\left(C+D\right)}\\
C &= \frac{p}{|\alpha|}\frac{1}{p-1}\exp\left(-\frac{|\alpha|^2}{2}\right)\\
D &= \sqrt{\frac{\pi}{2}}\left(1+\mathrm{erf}\left(\frac{|\alpha|}{\sqrt{2}}\right)\right)
\end{aligned}
$$

Coefficients μ_0 and σ are the first and the second moments of the Gaussian part in the CB function, and

two additional variables commonly denoted p and α, are responsible for the degree of the power-law tail and the point at which the function flips from the Gaussian to a power law. Term N and its components C and D are responsible for the normalization of the CB function.

Signal functions are first fit to the MC simulations of three $\Upsilon(n\mathrm{S})$ states and the parameters of the fits are studied as a function of $p_{\mathrm{T}}^{\mu\mu}$. Fits with constraints determined from the MC simulations are then applied to the data. Parameters that cannot be precisely extracted from the data, namely p, α, and ω, are fixed to the values obtained from simulations. For other parameters, the $p_{\mathrm{T}}^{\mu\mu}$ dependencies found in the simulated events are replaced with $p_{\mathrm{T}}^{\mu\mu}$ dependencies found in the data. Overall good agreement for fit parameters is found between the data and MC simulation. Finally, in the fits that are further used in the analysis only mass positions of the $\Upsilon(n\mathrm{S})$ peaks, their yields $N_{\Upsilon(n\mathrm{S})}$, and N_{bkg} are left as free parameters. All others are parametrized as smooth functions of $p_{\mathrm{T}}^{\mu\mu}$ and are fixed in the fits to the invariant mass. Peak positions are left free because they are fully consistent with weak dependencies observed in the MC without being constrained. This procedure significantly reduced statistical uncertainties in the fits and correlations between the fit parameters that are left free.

An example of the fit is shown in the left panel of Figure 1 which presents the breakdown of different contributions, determined from the fit to the data.

The charged particle multiplicity and kinematic distributions, generally denoted as P, are measured in the data in 5 di-muon invariant mass intervals $[8.2, 9.0]$, $[9.1, 9.7]$, $[9.8, 10.1]$, $[10.2, 10.6]$, $[11.0, 11.5]$ given in units of GeV and denoted in the left panel of Figure 1 as $m_n^{\mu\mu}$, where $n = 0 - 4$. Distributions in the lower and upper intervals $P(m_0^{\mu\mu})$ and $P(m_4^{\mu\mu})$ are dominated by background and the three middle intervals have significant contributions coming from one of the $\Upsilon(n\mathrm{S})$ states. Several examples of $P(m_n^{\mu\mu})$ measured for n_{ch} are shown in the right panel of Figure 1 with open markers.

Fits shown in the left panel allow determining signal and background contributions in the intervals $n = 0 - 4$ to disentangle distributions associated with different $\Upsilon(n\mathrm{S})$ states. Charged particle distributions coming from collisions with $\Upsilon(n\mathrm{S})$ in the mass intervals $m_k^{\mu\mu}$ with $n = k$ are denoted as s_n and contributions in the intervals $n \neq k$ as f_{nk}, they are calculated according to Eq. (3).

$$\begin{aligned} s_n &= \frac{\int_{m_n^{\mu\mu}} N_{\Upsilon(n\mathrm{S})} F_n\,(m)\,dm}{\int_{m_n^{\mu\mu}} \mathrm{fit}\,(m)\,dm} \\ f_{nk} &= \frac{\int_{m_n^{\mu\mu}} N_{\Upsilon(k\mathrm{S})} F_k\,(m)\,dm}{\int_{m_n^{\mu\mu}} \mathrm{fit}\,(m)\,dm} \end{aligned} \tag{3}$$

To assess the background contribution underneath the $\Upsilon(n\mathrm{S})$ peaks, the side-band subtraction method [35] is used. The contribution of the background in the n-th mass interval is taken as a weighted sum $k_n P_0 + (1 - k_n) P_4$ of the background distributions in mass intervals $m_0^{\mu\mu}$ and $m_4^{\mu\mu}$. Coefficient k_n is calculated according to Eq. 4.

$$k_n = \frac{\langle F_{\mathrm{bkg}}\,(m)\rangle|_{m_4^{\mu\mu}} - \langle F_{\mathrm{bkg}}\,(m)\rangle|_{m_n^{\mu\mu}}}{\langle F_{\mathrm{bkg}}\,(m)\rangle|_{m_4^{\mu\mu}} - \langle F_{\mathrm{bkg}}\,(m)\rangle|_{m_0^{\mu\mu}}} \tag{4}$$

Thus $P(m_n^{\mu\mu})$ distributions measured in 5 mass intervals can be presented in the form of a matrix that links them to the contributions coming from $\Upsilon(n\mathrm{S})$ collisions as well as from the background in the low- and

high-mass background intervals. This is given by Eq. (5).

$$\begin{pmatrix} P(m_0^{\mu\mu}) \\ P(m_1^{\mu\mu}) \\ P(m_2^{\mu\mu}) \\ P(m_3^{\mu\mu}) \\ P(m_4^{\mu\mu}) \end{pmatrix} = \begin{pmatrix} 1-f_{01} & f_{01} & 0 & 0 & 0 \\ k_1\,(1-s_1) & s_1 & 0 & 0 & (1-k_1)\,(1-s_1) \\ k_2\,(1-s_2-f_{21}-f_{23}) & f_{21} & s_2 & f_{23} & (1-k_2)\,(1-s_2-f_{21}-f_{23}) \\ k_3\,(1-s_3-f_{32}) & 0 & f_{32} & s_3 & (1-k_3)\,(1-s_3-f_{32}) \\ 0 & 0 & 0 & 0 & 1 \end{pmatrix} \begin{pmatrix} P_0 \\ P(\Upsilon(1\mathrm{S})) \\ P(\Upsilon(2\mathrm{S})) \\ P(\Upsilon(3\mathrm{S})) \\ P_4 \end{pmatrix} \quad (5)$$

There are matrix elements that are explicitly set to zero, reflecting the fact that the contribution of some physics processes to certain mass intervals are minimal and neglected. This matrix can be inverted to determine $P(\Upsilon(n\mathrm{S}))$ from $P(m_n^{\mu\mu})$ measured in the data.

Examples of the background-dominated distributions for n_{ch} in mass intervals $m_0^{\mu\mu}$ and $m_4^{\mu\mu}$ that are shown with triangles in the right panel of Figure 1 are seen to be close to each other, in spite of the fact that $P(m_0^{\mu\mu})$ has a small admixture f_{01} of the contribution $P(\Upsilon(1\mathrm{S}))$. This supports using the side-band subtraction method to reliably determine the shape of the background n_{ch} distributions at any $m^{\mu\mu}$. Transformation by the matrix given by Eq 5 can be seen as the transition between the curves with open and closed markers of the same shape. These are shown for $m_1^{\mu\mu}$ and $m_3^{\mu\mu}$ intervals as having the largest and the smallest signal contributions, respectively. n_{ch} distributions for the three $\Upsilon(n\mathrm{S})$ states are shown with full markers. These distributions have visibly different mean values. All n_{ch} distributions have contributions coming from the PU that is shown only for $\Upsilon(3\mathrm{S})$ with hatched markers because all PU contributions have the same shape.

The accuracy of the procedure is checked using pseudo-experiments. High-statistics MC samples are produced for all signal n_{ch} distributions and for the background. Shapes of the simulated distributions in the pseudo-experiment are matched to be close to the data. Those distributions are then used to produce distributions $P(m_n^{\mu\mu})$ that are then used as an input to the procedure described above. This is done for all $p_{\mathrm{T}}^{\mu\mu}$ measured in the analysis. At most, 1% deviations are observed for the three $\Upsilon(n\mathrm{S})$ states from the simulated signal distributions. The difference between reconstructed and actual values is included in the systematic uncertainties.

Fits and the background removal procedure are performed in each $p_{\mathrm{T}}^{\mu\mu}$ interval and for each trigger. The PU contribution varies with $p_{\mathrm{T}}^{\mu\mu}$ due to the changing mixture of triggers, but is otherwise constant in $m^{\mu\mu}$. Kinematic distributions for $\Upsilon(n\mathrm{S})$ and for the PU contribution measured with different triggers in each $p_{\mathrm{T}}^{\mu\mu}$ interval are summed up and subtracted from each other. For measuring $\langle n_{\mathrm{ch}} \rangle$ distributions, they are first averaged and then subtracted.

There are three primary sources of systematic uncertainties that affect the charged particle multiplicity and kinematic distributions measured in the analysis. The first includes factors related to the performance of the ID tracking system - material uncertainties and the physics model used in simulation [36]. The second source of systematic uncertainties, which is the dominant contribution in the total uncertainty at low $p_{\mathrm{T}}^{\mu\mu}$, includes factors coming from the uncertainties and assumptions made in the $\Upsilon(n\mathrm{S})$ signal extraction. They are evaluated by varying the parameters of the fitting function, by changing the limits of invariant mass intervals shown in the left panel of Figure 1, where the charged distributions are extracted, and by performing the analysis in $|y^{\mu\mu}| < 1.05$ where the detector momentum resolution for the muons is higher. In addition, the signal extraction procedure is tested using MC-based pseudo-experiments, which have distributions closely matched to the data. The last source of systematic uncertainties includes PU subtraction, detector stability and misreconstructed track production. Since the PU conditions varied significantly over the time of the data taking, these are considered together and assigned a common uncertainty. This uncertainty is studied by examining collisions with different PU conditions and evaluating

residual discrepancies between the expectation based on the PU track estimator [37] and the mean number of measured tracks. Since the sources of all uncertainties are independent, the resulting uncertainty is obtained by adding their values in quadrature. The resulting total systematic uncertainty depends on the state of the $\Upsilon(n\mathrm{S})$ and $p_{\mathrm{T}}^{\mu\mu}$. Uncertainties are propagated on all measured variables and are presented for $\langle n_{\mathrm{ch}} \rangle$ in Table 1.

	$p_{\mathrm{T}}^{\mu\mu} \leq 4$ GeV	$4 < p_{\mathrm{T}}^{\mu\mu} \leq 12$ GeV	$12 < p_{\mathrm{T}}^{\mu\mu} \leq 30$ GeV	$p_{\mathrm{T}}^{\mu\mu} > 30$ GeV
$\Upsilon(1\mathrm{S})$	0.5 – 0.6	0.5 – 0.7	0.7 – 0.8	0.8 – 0.9
$\Upsilon(2\mathrm{S})$	0.6 – 0.6	0.5 – 0.7	0.7 – 0.8	0.8 – 1.0
$\Upsilon(3\mathrm{S})$	0.9 – 1.3	0.5 – 0.8	0.7 – 0.8	0.8 – 0.9
$\Upsilon(1\mathrm{S}) - \Upsilon(2\mathrm{S})$	0.11 – 0.15	0.06 – 0.10	0.12 – 0.21	0.2 – 0.5
$\Upsilon(1\mathrm{S}) - \Upsilon(3\mathrm{S})$	0.6 – 0.9	0.14 – 0.36	0.14 – 0.15	0.16 – 0.19

Table 1: Systematic uncertainties for measurements of $\langle n_{\mathrm{ch}} \rangle$ and their differences for different $\Upsilon(n\mathrm{S})$ states and for the difference between $\langle n_{\mathrm{ch}} \rangle$ measured for $\Upsilon(1\mathrm{S}) - \Upsilon(n\mathrm{S})$. The values are the number of charged particles with $0.5 \leq p_{\mathrm{T}} < 10$ GeV and $|\eta| < 2.5$.

4 Results

Figure 2 shows kinematic distributions of charged particles measured in collisions with $\Upsilon(n\mathrm{S})$ states. The left panel shows the p_{T} distributions and the right panel distributions of the azimuthal angle between the directions of the particles and the Υ-meson ($\Delta\phi$). Cross-shaped markers show distributions measured in collisions with $\Upsilon(1\mathrm{S})$ meson, whereas other markers show the *subtracted* distributions, i.e., the differences between the results measured in collisions with $\Upsilon(1\mathrm{S})$ and higher $\Upsilon(n\mathrm{S})$ states, $\Upsilon(1\mathrm{S}) - \Upsilon(2\mathrm{S})$ with open markers and $\Upsilon(1\mathrm{S}) - \Upsilon(3\mathrm{S})$ with full markers. The distributions are shown for several intervals of $p_{\mathrm{T}}^{\mu\mu}$.

Predictions from Pythia 8 MC simulations of the same quantities are also shown as lines. Simulated results for the subtracted distributions are first scaled to have the integral as in the data with the same $\Upsilon(n\mathrm{S})$ state and then subtracted from each other. Solid lines are Pythia 8 predictions that include feed-down decays [38], which are decays of a higher mass particle to a lower-mass particle, between different $\Upsilon(n\mathrm{S})$ states, and dashed lines are the same predictions but excluding these feed-down events.

The charged particle p_{T} distributions in $\Upsilon(1\mathrm{S})$ collisions get significantly harder with increasing Υ momentum. Also the $\Delta\phi$ distributions develop a "near-side" peak around $\Delta\phi = 0$, and an "away-side" peak around $\Delta\phi = \pi$. These features which reflect the presence of a jet are qualitatively expected and the Pythia 8 prediction generally reproduces them well. However, the simulations have less activity than data at lower $\Upsilon(1\mathrm{S})$ $p_{\mathrm{T}}^{\mu\mu}$, and underestimate the near-side region of the $\Delta\phi$ distribution. A similar mismatch between data and Pythia8 was reported in Ref. [39]. The transverse momentum distributions of charged particles are softer than in the data, which may be related to the deficit of particles in the near-side region.

In all measured $p_{\mathrm{T}}^{\mu\mu}$ intervals, the subtracted distributions are above zero. Up to the highest measured $p_{\mathrm{T}}^{\mu\mu}$ interval, the subtracted p_{T} distributions are more consistent in shape with distributions measured in the lowest $p_{\mathrm{T}}^{\mu\mu}$ interval of $\Upsilon(1\mathrm{S})$, rather than to the distributions in their $p_{\mathrm{T}}^{\mu\mu}$ interval. Above 30 GeV the $\Upsilon(1\mathrm{S}) - \Upsilon(3\mathrm{S})$ subtracted p_{T}-distribution gets harder, and peaks appear around $\Delta\phi = 0$ and $\Delta\phi = \pi$. The Pythia 8 predictions, if feed-down decays from excited Υ states to lower-level Υ states are included, show similar features to the data.

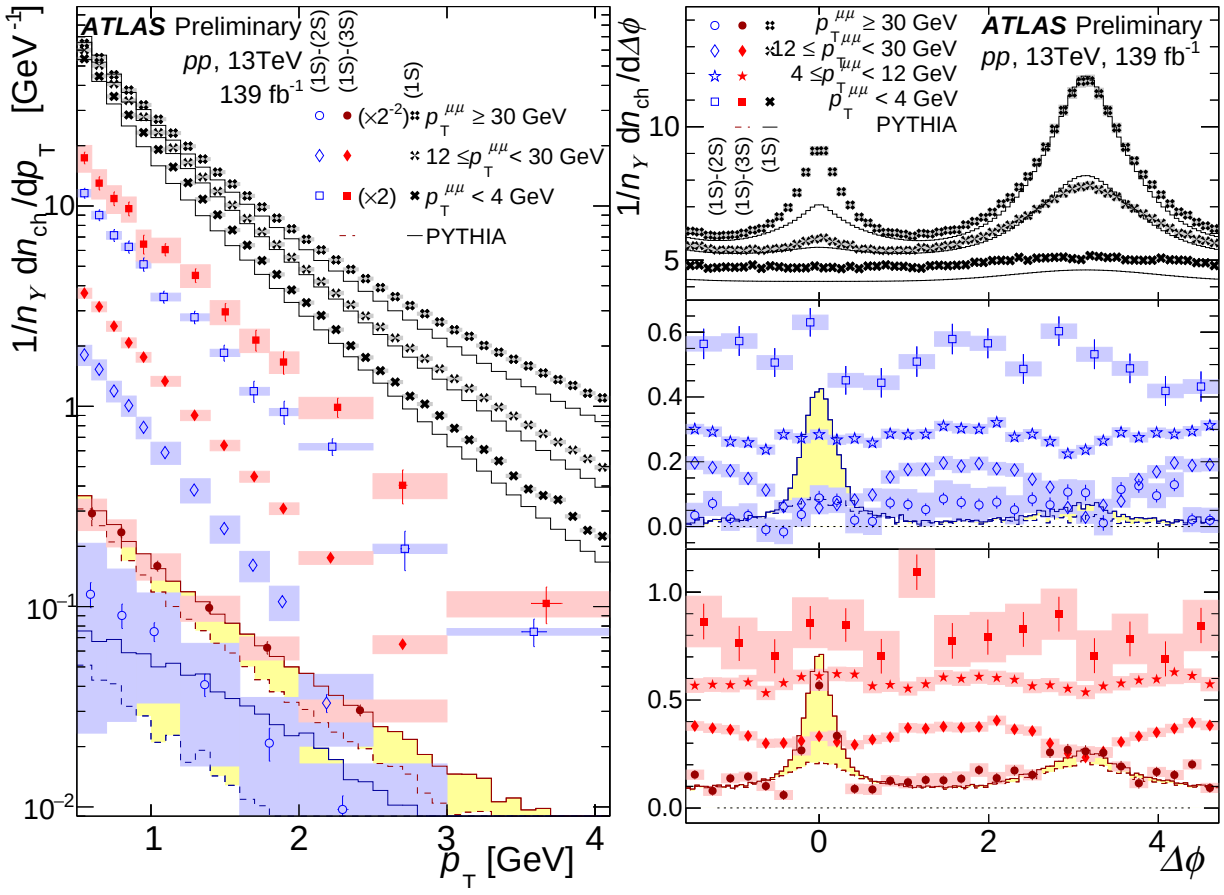

Figure 2: Distributions of charged particles in p_{T} (left) and $\Delta\phi$ (right) in collisions with different Υ-meson $p_{\mathrm{T}}^{\mu\mu}$. Cross-shaped markers correspond to $\Upsilon(1\mathrm{S})$, open markers to $\Upsilon(1\mathrm{S}) - \Upsilon(2\mathrm{S})$ and full markers to $\Upsilon(1\mathrm{S}) - \Upsilon(3\mathrm{S})$, respectively. Pythia 8 predictions are plotted in black solid lines for $\Upsilon(1\mathrm{S})$. In the subtracted distributions, Pythia 8 simulations are plotted in colored lines for the $p_{\mathrm{T}}^{\mu\mu} \geq 30$ GeV selections. Solid and dashed lines are Pythia 8 predictions with and without $\Upsilon(n\mathrm{S}) \rightarrow \Upsilon(\mathrm{mS})$ contributions respectively. Regions filled with yellow represent the difference between the predictions with and without feed-down decays. Bars and boxes are statistical and systematic uncertainties, respectively. p_{T} distributions of subtracted results are scaled for plot clarity, as indicated in the legend.

There are other non-uniformities in subtracted $\Delta\phi$ distributions, which become pronounced in $12 \leq p_{\mathrm{T}}^{\mu\mu} < 30$ GeV momentum interval. Several physics processes may contribute to this, including feed-down decays from higher $\Upsilon(n\mathrm{S})$ into $\Upsilon(1\mathrm{S})$, feed-down decays from $\chi_b(m\mathrm{P})$ mesons into $\Upsilon(n\mathrm{S})$ (which are not accounted for in the Pythia 8 predictions), slightly more energetic jets containing lighter Υ mesons and other factors. Nevertheless, in the region around $\Delta\phi = \pm\pi/2$, the difference in the $\mathrm{d}n_{\mathrm{ch}}/\mathrm{d}\Delta\phi$ always remains above zero for both $\Upsilon(1\mathrm{S}) - \Upsilon(2\mathrm{S})$ and $\Upsilon(1\mathrm{S}) - \Upsilon(3\mathrm{S})$ distributions. This suggests that the differences in the soft particle production observed in this region may not arise from the hard scattering process producing the Υ meson.

The mean number of charged particles with transverse momentum between 0.5 and 10 GeV measured in the pseudorapidity range $|\eta| < 2.5$ in events with reconstructed $\Upsilon(n\mathrm{S})$ mesons are shown in Figure 3 as a function of Υ's $p_{\mathrm{T}}^{\mu\mu}$. The upper panel shows the results for the three measured Υ states, and the lower panel shows the differences $\Upsilon(1\mathrm{S})$ less $\Upsilon(2\mathrm{S})$, and $\Upsilon(1\mathrm{S})$ less $\Upsilon(3\mathrm{S})$ states. The Figure shows significant

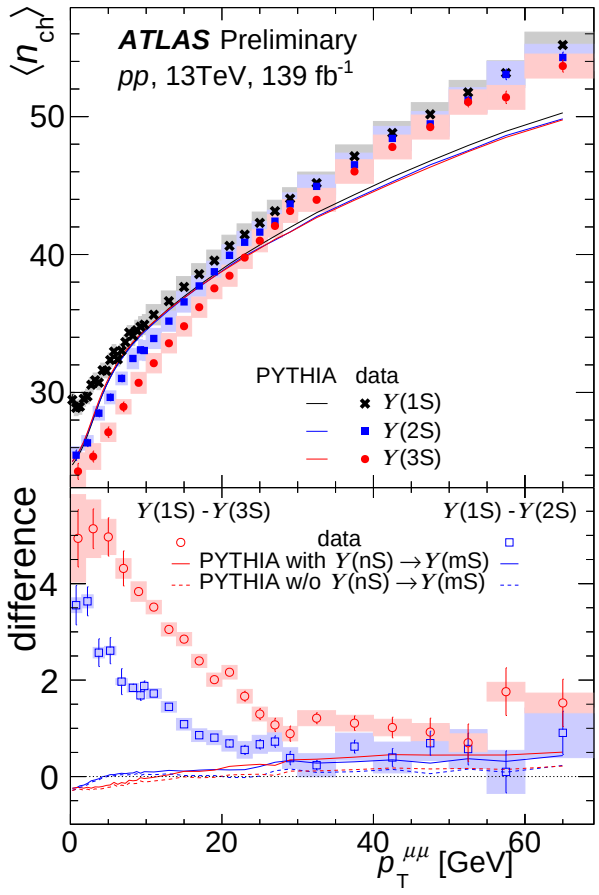

Figure 3: The mean number of charged particles with $0.5 < p_{\mathrm{T}} < 10$ GeV and $|\eta| < 2.5$ in events with $\Upsilon(n\mathrm{S})$ mesons (top) and difference of this quantity between the excited and ground $\Upsilon(n\mathrm{S})$ state (bottom). Pythia 8 predictions with (solid) and without (dashed) $\Upsilon(n\mathrm{S}) \to \Upsilon(\mathrm{mS})$ contributions are shown by solid and dashed lines respectively. Statistical uncertainties are shown with error bars, boxes are systematic uncertainties.

differences in $\langle n_{\mathrm{ch}} \rangle$. Unlike the data, the Pythia 8 prediction shows very similar particle multiplicity for all three Υ states. This conclusion is unchanged by changing the color reconnection scheme in the Pythia 8 simulation.

At the lowest measured p_{T}, the difference in $\langle n_{\mathrm{ch}} \rangle$ for $\Upsilon(1\mathrm{S}) - \Upsilon(2\mathrm{S})$ is 3.6 ± 0.4 and for $\Upsilon(1\mathrm{S}) - \Upsilon(3\mathrm{S})$ it is 4.9 ± 1.1, where the uncertainties correspond to systematic and statistical uncertainties added in quadrature. The $p_{\mathrm{T}}^{\mu\mu}$ dependences of the differences between the excited and ground states are similar for both excited states. However, large uncertainties in the $\Upsilon(3\mathrm{S})$ measurement at the lowest $p_{\mathrm{T}}^{\mu\mu}$ do not allow to draw definite conclusions whether the shapes are exactly the same. The differences in $\langle n_{\mathrm{ch}} \rangle$ gets smaller with increasing $p_{\mathrm{T}}^{\mu\mu}$ but remain above zero even for the highest measured momentum. The Pythia 8 predictions of the difference in the mean number of charged particles in excited Υ states and $\Upsilon(1\mathrm{S})$ are also slightly positive for higher $p_{\mathrm{T}}^{\mu\mu}$, due to the differences in mass of the $\Upsilon(n\mathrm{S})$ states as well as from feed-down decays.

5 Summary

The ATLAS experiment has measured the multiplicity and kinematic distributions of charged hadrons produced in pp collisions at $\sqrt{s}$ = 13 TeV in events with Υ mesons. A significant difference in the charged particle multiplicity is observed in collisions with different $\Upsilon(n\mathrm{S})$ states that is not explained by Pythia 8 MC event generator. In the lowest measured $p_{\mathrm{T}}^{\mu\mu}$ intervals, collisions with $\Upsilon(1\mathrm{S})$ contain $\langle n_{\mathrm{ch}} \rangle = 29.5 \pm 0.7$ charged hadrons, whereas in collisions with $\Upsilon(2\mathrm{S})$ and $\Upsilon(3\mathrm{S})$ there are 3.6 ± 0.4 ($12 \pm 1\%$) and 4.9 ± 1.1 ($17 \pm 4\%$) fewer particles, respectively. The uncertainties are statistical and systematic added in quadrature. Differences in $\langle n_{\mathrm{ch}} \rangle$ across $\Upsilon(n\mathrm{S})$ states are strongly momentum-dependent: they decrease with increasing $p_{\mathrm{T}}^{\mu\mu}$ of the $b\bar{b}$ state and are reduced at higher momenta. This note provides new data for models that describe Upsilon production and dynamics in high-multiplicity pp collisions.

Appendix

Figure 4 is analog of Figure 2 with one additional $p_{\mathrm{T}}^{\mu\mu}$ interval measurement in the left panel.

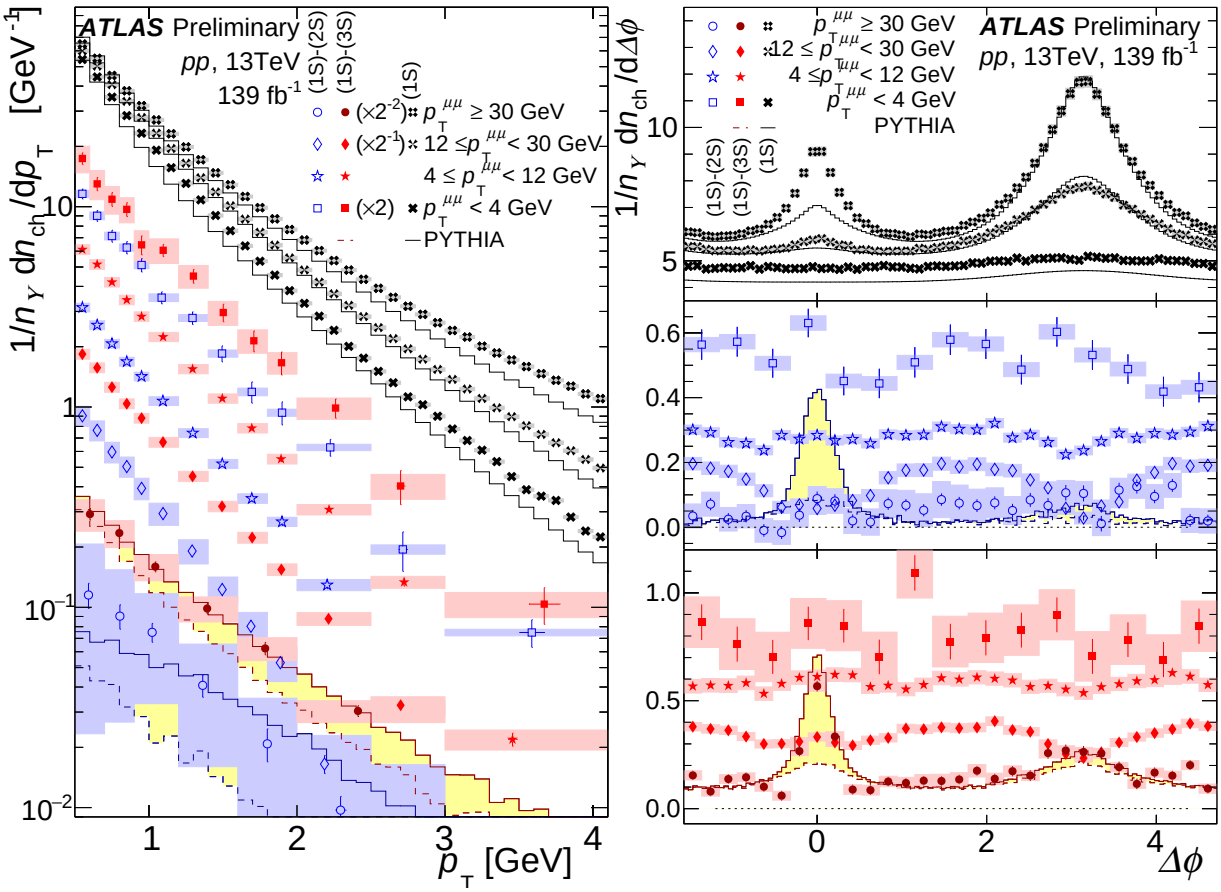

Figure 4: Distributions of charged particles in p_{T} (left) and $\Delta\phi$ (right) in collisions with different Υ-meson $p_{\mathrm{T}}^{\mu\mu}$. Cross-shaped markers correspond to $\Upsilon(1\mathrm{S})$, open markers to $\Upsilon(1\mathrm{S}) - \Upsilon(2\mathrm{S})$ and full markers to $\Upsilon(1\mathrm{S}) - \Upsilon(3\mathrm{S})$ respectively. Solid and dashed lines are Pythia 8 simulations with and without $\Upsilon(n\mathrm{S}) \to \Upsilon(\mathrm{mS})$ contributions respectively. Regions filled with yellow represent the difference between Pythia predictions with and without feed-down decays. Bars and boxes are statistical and systematic uncertainties, respectively. p_{T} distributions of subtracted results are scaled for plot clarity, as indicated in the legend.

References

[1] ATLAS Collaboration, *Underlying event characteristics and their dependence on jet size of charged-particle jet events in pp collisions at $\sqrt{s}$ = 7 TeV with the ATLAS detector*, Phys. Rev. D **86** (2012) 072004, arXiv: 1208.0563 [hep-ex] (cit. on p. 2).

[2] ATLAS Collaboration, *Measurement of distributions sensitive to the underlying event in inclusive Z-boson production in pp collisions at $\sqrt{s}$ = 7 TeV with the ATLAS detector*, Eur. Phys. J. C **74** (2014) 3195, arXiv: 1409.3433 [hep-ex] (cit. on p. 2).

[3] ATLAS Collaboration, *Measurement of charged-particle distributions sensitive to the underlying event in $\sqrt{s}$ = 13 TeV proton-proton collisions with the ATLAS detector at the LHC*, JHEP **03** (2017) 157, arXiv: 1701.05390 (cit. on pp. 2, 4).

[4] ATLAS Collaboration, *Measurement of the $\Upsilon(1S)$ production cross-section in pp collisions at $\sqrt{s}$ = 7 TeV in ATLAS*, Phys. Lett. B **705** (2011) 9, arXiv: 1106.5325 (cit. on p. 2).

[5] ATLAS Collaboration, *Measurement of Υ production in 7 TeV pp collisions at ATLAS*, Phys. Rev. D **87** (2013) 052004, arXiv: 1211.7255 (cit. on p. 2).

[6] CMS Collaboration, *Measurement of the $\Upsilon(1S)$, $\Upsilon(2S)$, and $\Upsilon(3S)$ Cross Sections in pp Collisions at $\sqrt{s}$ = 7 TeV*, Phys. Lett. B **727** (2013) 101, arXiv: 1303.5900 (cit. on p. 2).

[7] CMS Collaboration, *Measurements of the $\Upsilon(1S)$, $\Upsilon(2S)$, and $\Upsilon(3S)$ differential cross sections in pp collisions at $\sqrt{s}$ = 7 TeV*, Phys. Lett. B **749** (2015) 14, arXiv: 1501.07750 (cit. on p. 2).

[8] CMS Collaboration, *Measurement of quarkonium production cross sections in pp collisions at $\sqrt{s}$ = 13 TeV*, Phys. Lett. B **780** (2018) 251, arXiv: 1710.11002 (cit. on p. 2).

[9] LHCb Collaboration, *Production of J/psi and Upsilon mesons in pp collisions at sqrt(s) = 8 TeV*, JHEP **06** (2013) 064, arXiv: 1304.6977 (cit. on p. 2).

[10] LHCb Collaboration, *Forward production of Υ mesons in pp collisions at $\sqrt{s}$ = 7 and 8 TeV*, JHEP **11** (2015) 103, arXiv: 1509.02372 (cit. on p. 2).

[11] LHCb Collaboration, *Measurement of Υ production in pp collisions at $\sqrt{s}$= 13 TeV*, JHEP **07** (2018) 134, [Erratum: JHEP 05, 076 (2019)], arXiv: 1804.09214 (cit. on p. 2).

[12] J.-P. Lansberg, *New Observables in Inclusive Production of Quarkonia*, Phys. Rept. **889** (2020) 1, arXiv: 1903.09185 [hep-ph] (cit. on p. 2).

[13] A. Andronic et al., *Heavy-flavour and quarkonium production in the LHC era: from proton–proton to heavy-ion collisions*, Eur. Phys. J. C **76** (2016) 107, arXiv: 1506.03981 (cit. on p. 2).

[14] CMS Collaboration, *Event Activity Dependence of $\Upsilon(nS)$ Production in $\sqrt{s_{NN}}$ = 5.02 TeV p+Pb and $\sqrt{s}$ = 2.76 TeV pp Collisions*, JHEP **04** (2014) 103, arXiv: 1312.6300 (cit. on p. 2).

[15] CMS Collaboration, *Investigation into the event-activity dependence of $\Upsilon(nS)$ relative production in proton-proton collisions at $\sqrt{s}$ = 7 TeV*, JHEP **11** (2020) 001, arXiv: 2007.04277 (cit. on p. 2).

[16] ATLAS Collaboration, *Measurement of long-range two-particle azimuthal correlations in Z-boson tagged pp collisions at $\sqrt{s}$ = 8 and 13 TeV*, Eur. Phys. J. C **80** (2020) 64, arXiv: 1906.08290 (cit. on pp. 2, 4, 5).

[17] ATLAS Collaboration, *The ATLAS Experiment at the CERN Large Hadron Collider*, JINST **3** (2008) S08003 (cit. on p. 3).

[18] ATLAS Collaboration, *ATLAS Insertable B-Layer: Technical Design Report*, ATLAS-TDR-19; CERN-LHCC-2010-013, 2010, URL: https://cds.cern.ch/record/1291633 (cit. on p. 3), Addendum: ATLAS-TDR-19-ADD-1; CERN-LHCC-2012-009, 2012, URL: https://cds.cern.ch/record/1451888.

[19] B. Abbott et al., *Production and integration of the ATLAS Insertable B-Layer*, JINST **13** (2018) T05008, arXiv: 1803.00844 [physics.ins-det] (cit. on p. 3).

[20] ATLAS Collaboration, *Performance of the ATLAS trigger system in 2015*, Eur. Phys. J. C **77** (2017) 317, arXiv: 1611.09661 [hep-ex] (cit. on p. 3).

[21] ATLAS Collaboration, *The ATLAS Collaboration Software and Firmware*, ATL-SOFT-PUB-2021-001, 2021, URL: https://cds.cern.ch/record/2767187 (cit. on p. 3).

[22] ATLAS Collaboration, *ATLAS data quality operations and performance for 2015–2018 data-taking*, JINST **15** (2020) P04003, arXiv: 1911.04632 [physics.ins-det] (cit. on p. 4).

[23] T. Sjostrand, S. Mrenna and P. Z. Skands, *A Brief Introduction to PYTHIA 8.1*, Comput. Phys. Commun. **178** (2008) 852, arXiv: 0710.3820 (cit. on p. 4).

[24] ATLAS Collaboration, *ATLAS Pythia 8 tunes to 7 TeV data*, ATL-PHYS-PUB-2014-021, URL: https://cds.cern.ch/record/1966419 (cit. on p. 4).

[25] P. Golonka and Z. Was, *PHOTOS Monte Carlo: A Precision tool for QED corrections in Z and W decays*, Eur. Phys. J. C **45** (2006) 97, arXiv: hep-ph/0506026 (cit. on p. 4).

[26] N. Davidson, T. Przedzinski and Z. Was, *PHOTOS interface in C++: Technical and Physics Documentation*, Comput. Phys. Commun. **199** (2016) 86, arXiv: 1011.0937 (cit. on p. 4).

[27] S. Agostinelli et al., *GEANT4–a simulation toolkit*, Nucl. Instrum. Meth. A **506** (2003) 250 (cit. on p. 4).

[28] ATLAS Collaboration, *The ATLAS Simulation Infrastructure*, Eur. Phys. J. C **70** (2010) 823, arXiv: 1005.4568 (cit. on p. 4).

[29] J. R. Christiansen and P. Z. Skands, *String Formation Beyond Leading Colour*, JHEP **08** (2015) 003, arXiv: 1505.01681 [hep-ph] (cit. on p. 4).

[30] ATLAS Collaboration, *Performance of the ATLAS Trigger System in 2015*, Eur. Phys. J. C **77** (2017) 317, arXiv: 1611.09661 (cit. on pp. 4, 5).

[31] ATLAS Collaboration, *Performance of the ATLAS muon triggers in Run 2*, JINST **15** (2020) P09015, arXiv: 2004.13447 (cit. on pp. 4, 5).

[32] A. Krasznahorkay, *Tools for Trigger Aware Analyses in Atlas*, tech. rep., CERN, 2010, URL: https://cds.cern.ch/record/1308441 (cit. on p. 4).

[33] ATLAS Collaboration, *Muon reconstruction performance of the ATLAS detector in proton–proton collision data at* $\sqrt{s}$ = 13 *TeV*, Eur. Phys. J. C **76** (2016) 292, arXiv: 1603.05598 (cit. on pp. 4, 5).

[34] ATLAS Collaboration, *Performance of the ATLAS Track Reconstruction Algorithms in Dense Environments in LHC Run 2*, Eur. Phys. J. C **77** (2017) 673, arXiv: 1704.07983 [hep-ex] (cit. on p. 5).

[35] ATLAS Collaboration,
Probing lepton flavour violation via neutrinoless $\tau \longrightarrow 3\mu$ decays with the ATLAS detector,
Eur. Phys. J. C **76** (2016) 232, arXiv: 1601.03567 (cit. on p. 7).

[36] ATLAS Collaboration, *Charged-particle distributions in $\sqrt{s} = 13$ TeV pp interactions measured with the ATLAS detector at the LHC*, Phys. Lett. B **758** (2016) 67, arXiv: 1602.01633 (cit. on p. 8).

[37] ATLAS Collaboration, *Measurement of long-range two-particle azimuthal correlations in Z-boson tagged pp collisions at $\sqrt{s} = 8$ and 13 TeV*, Eur. Phys. J. C **80** (2020) 64, arXiv: 1906.08290 (cit. on p. 9).

[38] S. Digal, P. Petreczky and H. Satz, *Quarkonium feed down and sequential suppression*,
Phys. Rev. D **64** (2001) 094015, arXiv: hep-ph/0106017 (cit. on p. 9).

[39] CMS Collaboration,
Fragmentation of jets containing a prompt J/ψ meson in PbPb and pp collisions at sNN=5.02TeV,
Phys. Lett. B **825** (2022) 136842, arXiv: 2106.13235 (cit. on p. 9).